

1 **Strain Hardening exponent and strain at maximum stress: steel rebar case**

2

3

4 **Abstract**

5

6 The typical distribution of steel used in developed countries, according to **World Steel Association**, attributes approximately
7 35% of total steel production in the world to the construction sector. Rebar steel consumption constitutes a significant
8 proportion of that figure. More in-depth knowledge regarding the behaviour of steels used in the production of rebar would be
9 advantageous. It has been shown that elasto-plastic behaviour greatly affects the behaviour of steel under seismic action. In
10 particular, the engineering strain at maximum engineering stress, A_{gt} , is gaining importance as the key ductility parameter in
11 the latest standards. Several authors have linked the value of A_{gt} to the Hollomon strain-hardening exponent, n . Three materials
12 have been tensile tested at room temperature, namely TEMPCORE[®] carbon steel, an austenitic, and duplex steel. In this paper,
13 it is shown that such a link is only valid when the local n value is computed at $A \rightarrow A_{gt}$ ($\varepsilon_z \rightarrow \varepsilon_{gt}$ in true values). In accordance
14 with the metallographic structure of rebar, the contrasting behaviour of the Hollomon strain-hardening exponent n versus ε_z is
15 described.

16

17 **Keywords**

18

19 Steel

20 Mechanical characterization

21 Thermomechanical processing

22 Plasticity

23 Hardening

24 EBSD

25

26

27 **Nomenclature**

28 Nomenclature follows the recommendations as per ISO 6892-1:2016 [1] and, when convenient, ASTM E6-09 [2]

29

Symbol	Units	Explanation
E	FL^{-2}	Young's modulus (modulus of elasticity in tension)
F	F	Axial force (load)
S	L^2	Instantaneous cross-sectional area
R	FL^{-2}	Engineering axial stress
$R_{p,0.2}$	FL^{-2}	Engineering yield strength computed to an offset strain of 0.2%
$R_{pm,0.2}$	FL^{-2}	Nominal engineering yield strength
R_m	FL^{-2}	Engineering axial strength at maximum force (also referred to as ultimate tensile strength)
A	dimensionless	Engineering axial strain
A_{gt}	dimensionless	Engineering axial strain at R_m
σ_z	FL^{-2}	True normal stress. For uniform strain, $\sigma_z = R(I + A)$
σ_y	FL^{-2}	True yield strength corresponding to $R_{p,0.2}$
σ_m	FL^{-2}	True tensile strength corresponding to R_m
ε_z	dimensionless	True axial strain. Can be computed as $\varepsilon_z = Ln(I+A)$
ε_{gt}	dimensionless	True axial strain corresponding to A_{gt}

30

31 **1. Introduction**

32

33 In the second half of the 19th century, reinforced concrete was first used to build the Lambot boat and Monier flowerpots.
 34 Structural applications began immediately and two patents were issued as the Hennebique and Monier systems [3]. In 1884, E.
 35 L. Ransome patented [4] the system of twisting square steel bars to increase strength and adhesion to the concrete. By the
 36 1940s, reinforcing steel consisted of smooth bars of 240 to 350 MPa in yield strength. The Ysteg Austrian system [5] presented
 37 up to 410 MPa, obtained through cold torsion plus the straining of two common steel bars. Other cold finished bars, such as
 38 Spanish Tetracero [5], gave high yield strengths and, consequently, elastic strains that could not be efficiently transmitted to
 39 the concrete, thereby causing cracks. By the end of the 1940s, the patenting of steel with ribs improved adhesion to the
 40 concrete [6]. Those bars were commonly produced by hot-rolling processes. High strengths were attained by means of
 41 increasing the content of carbon steel, but the joining of rebar by welding was not possible. On the other hand, cold straining,
 42 by rolling or drawing, increased strengths but produced less elongation.

43 Ductility issues are of paramount importance in withstanding seismic actions, increasing energy absorption, and preventing
 44 catastrophic structural failure [7,8,9,10,11,12]. In this respect, it has been shown that by increasing $R_m/R_{p,0.2}$ [13,14] or by
 45 reducing $R_{p,0.2}/R_{pm,0.2}$ [15], seismic action response can be improved. Current standard editions (Table I) implement those
 46 requirements along with a minimum value of A_{gt} [16], as criteria to rebar ductility classification.

47

Table I. Testing-related standards of selected rebar steel

	ISO	ASTM	BS
Rebar Product Standard	6935-2:2015 [17]	A615-16 [18]	BS 4449:2005[19]
Rebar Testing Standard	15630-1:2010 [20]	A370-17 [21]	BS EN ISO 15630-1:2010[22]
Metals Tensile Test Standard	6892-1:2016 [1]	E8-16 [23]	BS EN ISO 6892-1:2016[24]

48 In recent decades, the increasing concern regarding improvements in ductility has motivated rebar developments. Nowadays, a
 49 good deal of carbon steel rebar is produced by a hot-rolling controlled-cooling process registered as TEMPCORE® [25]. The
 50 final structure is a type of macroscopically divorced double-phase (DP) steel, where the outer coat consists of martensite, while
 51 the inner core is composed of a ferrite-pearlite structure.

52 Closely linked to the aforementioned ductility parameters is the rebar strain-hardening response. Even though several
 53 descriptive laws have been proposed [26,27], the Hollomon formulation originating from the 1950s [28], remains widely used
 54 today:

55
$$\sigma_z = K\varepsilon_z^n \tag{1}$$

56

57 In the original Hollomon paper, n , referred to as the hardening exponent, is considered to be a constant. Lower n values mean a
 58 lower rate of increase in stress as the strain increases. As a first approach, it may be said that, for a given level of strength (σ_y ,
 59 σ_m), the lower the n value falls, the higher the parameter ε_{gt} reaches. Nevertheless, an assumption of constant level (σ_y , σ_m),
 60 independently from the value of n , is unrealistic. In fact, σ_m is reached when the stress increase rate, directly related to the
 61 hardening exponent value, is lower than the rate of area shrinkage in the neck zone. According to Considère [29], at the onset
 62 of localized necking, which is where ε_{gt} is determined, the following holds:

$$dF = \sigma_z dS + S d\sigma_z \quad (2)$$

65 Furthermore, it can be shown from Eq. (2) that at the onset of localized necking:

$$\sigma_z = d\sigma_m / d\varepsilon_{gt} |_{\sigma_z = \sigma_m} \quad (3)$$

67 Substituting this into Eq. (1) yields:

$$\varepsilon_{gt} = n \quad (4)$$

69 It can be said that materials showing low hardening exponent values can easily experience necking in the presence of
 70 geometrical or microstructural inhomogeneities. On the other hand, when dealing with materials of high hardening exponent
 71 values, those incipient necking areas will harden, thereby preventing further shrinkage and extending the uniform strain
 72 behaviour to higher ε_{gt} values.

73 From the above discussion, a deeper knowledge of n values of rebar steel is worth attaining in order to better ascertain the
 74 ductility and seismic behaviour of these types of steel. An additional issue arises from the fact that the n value may change
 75 over the range of uniform plastic deformations. Several authors have proposed a behaviour known as double- n [30,31] or
 76 triple- n behaviour [32]. Other authors, including [33,34,35], have pointed out that the hardening exponent value is sensitive to
 77 changing deformation mechanisms active at different strain levels. Since the value of n as a function of ε_z is closely related to
 78 the ductility behaviour of rebar steels, then it is convenient to describe such relationships.

79 In this paper, the value of ε_{gt} is related to the strain-hardening exponent of the rebar material. Considering that those
 80 relationships are connected to hardening mechanisms, several rebar microstructures have been tested, including ferritic-
 81 martensitic, austenitic, and austeno-ferritic microstructures.

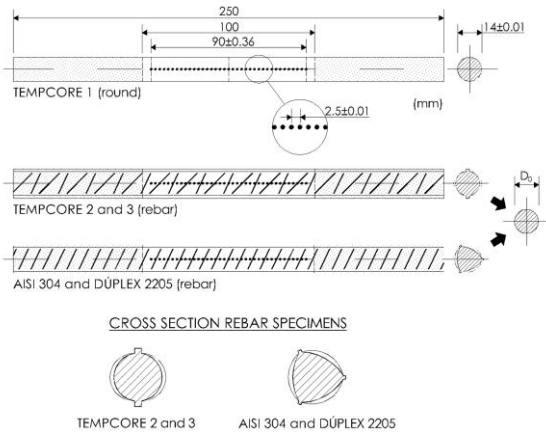
82 83 2. Material and methods

84 Three TEMPCORE[®] processed carbon steels and two cold-finished stainless grades have been tested (Fig. 1). One of the
 85 carbon steels was produced as plain round bars. The remaining two carbon steels were shaped as rebar, but show slightly
 86 different mechanical properties. The stainless steel rebar had austenitic and austeno-ferritic structures, respectively. Their
 87 chemical compositions are shown in Table II. Specimen numbers and microstructural properties are shown in Table III.

88 89 Table II. Chemical composition (%)

	C	Si	Mn	P	S	Cr	Ni	Mo	Cu	N	Sn	Ti	Co	C _{equ}
TEMPCORE [®] 1 (round)	0.15	0.16	0.65	0.027	0.040	0.16	0.10	0.02	0.46	0.009				0.33
TEMPCORE [®] 2 (rebar)	0.22	0.20	0.71	0.034	0.035	0.17	0.10	0.02	0.46	0.004	0.02			0.41
TEMPCORE [®] 3 (rebar)	0.18	0.12	0.73	0.023	0.034	0.16	0.15	0.03	0.44	0.012	0.02			0.38
AISI 304 (rebar)	0.05	0.27	1.44	0.030	0.002	18.24	8.21	0.26	0.28	0.05		0.005	0.14	
Duplex 2205 (rebar)	0.02	0.32	1.60	0.032	0.0014	22.45	4.66	3.28	0.12	0.17		0.009	0.034	

90



91

92 Figure 1. Geometrical properties of tested specimens

93

94

Table III. Number and properties of tested specimens

Material	N° specimens	Steel	Microstructure	$D_0^*(\text{mm})$
TEMPCORE [®] 1	8	Round	Ferritic	
TEMPCORE [®] 2	8	Rebar	Ferritic	13.85±0.02
TEMPCORE [®] 3	8	Rebar	Ferritic	13.93±0.03
AISI 304	8	Rebar	Austenitic	13.91±0.06
Duplex 2205	8	Rebar	Austeno-ferritic	13.82±0.04

95

96



97

98 **Figure 2. Tensile test of a TEMPCORE 2 rebar**

99 Tensile tests were carried out in accordance with ISO 15630-1:2010 [20] and ISO 6892-1:2016 standards [1]. Additionally, 20
 100 MPa.s⁻¹ was selected as the test speed during the elastic period. In determining Young modulus (E), a Class 1 extensometer
 101 was clamped down on the samples (Fig. 2). Plastic behaviour data was acquired while stretching at 0.167 mm s⁻¹. Mean values

102 of mechanical properties are shown in Table IV. Concerning TEMPCORE[®] specimens, all three materials comply with stress
 103 and strain parameters set out in European standard EN 1992:1-1 [36] for rebar 500C. On the other hand, there are no specific
 104 standards for stainless rebar. Several authors [37,38] have tested AISI 304 and Duplex 2205 rebar, obtaining concordant data
 105 with the results shown in Table IV.

106 Grain size was measured on typical micrographs using the Linear Intercept Method recommended by the ASTM standard E112
 107 [39] specification. Having determined the mean linear intercept grain size (m.l.i.) and based on the assumption of a spherical
 108 grain, the three-dimensional grain diameter d is given by $d = 3(\text{m.l.i.})/2$. This three-dimensional grain diameter d is commonly
 109 used to correlate the grain size with mechanical properties (Table IV).

110
 111

Table IV. Mechanical properties (mean values)

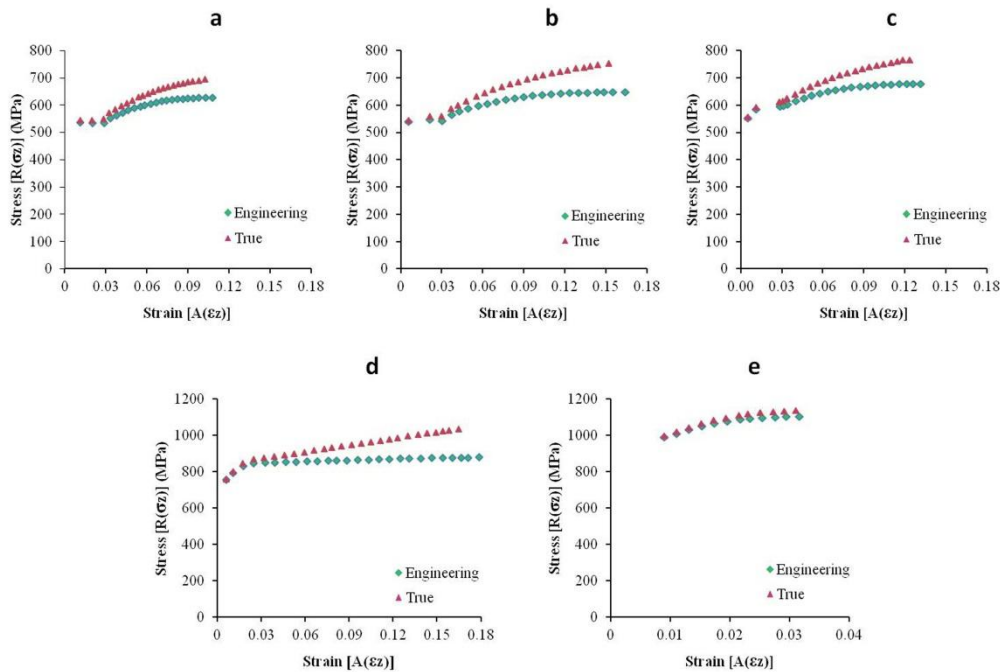
Material	$R_{p,0.2}$ (MPa)	R_m (MPa)	$R_m/R_{p,0.2}$	ϵ_{gt}	E (GPa)
TEMPCORE [®] 1 (round)	518.70±7.18	627.26±2.85	1.21±0.02	0.106±0.003	195
TEMPCORE [®] 2 (rebar)	521.46±11.13	647.19±1,37	1.24±0,03	0.156±0.008	200
TEMPCORE [®] 3 (rebar)	546.04±3.98	678.31±2.83	1.24±0.01	0.126±0.005	187
AISI 304 (rebar)	750.80±12.86	879.16±6.36	1.17±0.01	0.178±0.006	197
Duplex 2205 (rebar)	983.54±19.35	1103.45±6.88	1.12±0.02	0.032±0.021	195

112 Microstructural analyses were carried out using a scanning electron microscope (Zeiss Auriga) at 30 kV. The electron
 113 backscatter diffraction (EBSD) measurements were collected through a detector (Oxford Nordlys Nano) at 20 kV and 70°
 114 sample tilt, 7 mm working distance, and 60 μ A beam intensity.

115

116 3. Results

117 The tensile test results are shown in Fig. 3. Curves are drawn by computing the mean value of the stresses needed to reach a
 118 certain plastic strain for each of the eight samples tested. Only the uniform strain behaviour has been considered, that is, curves
 119 have been plotted up to the eight samples mean A_{gt} (ϵ_{gt}) values.



120

121 Figure 3. Experimental results R vs. A (open symbols), and σ_z .vs. ϵ_z (full symbols) of: (a) TEMPCORE[®] 1 (round); (b)
 122 TEMPCORE[®] 2 (rebar); (c) TEMPCORE[®] 3 (rebar); (d) AISI 304; and (e) Duplex 2205 samples.

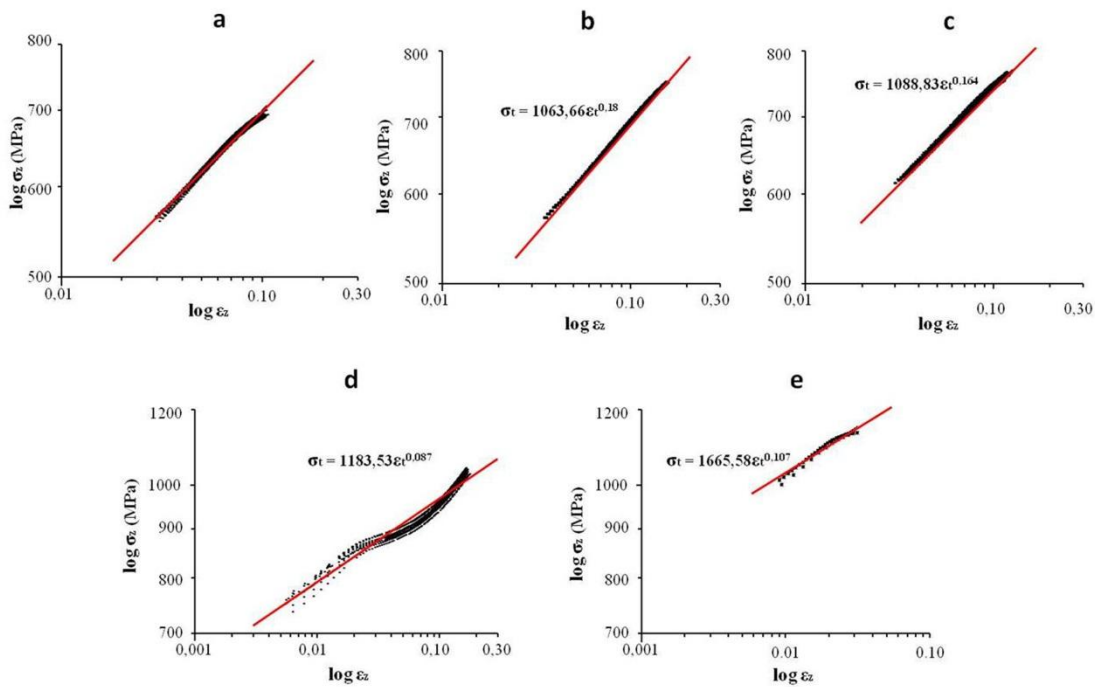
123 Fitting experimental data to Hollomon formulation [28] (Eq. (1)) requires a previous decision regarding the initial point of
 124 homogeneous plastic hardening. According to several authors [40] a strain value slightly above that of the minimum yield
 125 stress should be considered. To this end, the strain corresponding to an absolute deformation of 0.4 mm in excess of that of the
 126 last minimum in yield stress has been selected. Table V lists the Hollomon equation mean constants corresponding to all the
 127 individual samples tested, grouped in terms of materials. Typical R^2 fitting parameter and mean ε_{gt} values are also shown. Fig.
 128 4 shows log-log plots of ε_z - σ_z experimental values, along with the Hollomon equation best fit when all the experimental values
 129 for each material are considered at the same fit.

130 Table V. Hollomon equation constants and ε_{gt} value

Material	$K(\text{mean})$	$n(\text{mean})$	R^{2*}	ε_{gt}
TEMPCORE [®] 1 (round)	1049.65±16.23	0.176±0.006	0.989	0.101±0.003
TEMPCORE [®] 2 (rebar)	1064.73±5.92	0.180±0.004	0.995	0.145±0.007
TEMPCORE [®] 3 (rebar)	1090.22±6.81	0.164±0.003	0.994	0.119±0.004
AISI 304	1183.98±6.08	0.087±0.003	0.945	0.164±0.005
Duplex 2205	1671.57±30.10	0.108±0.007	0.884	0.032±0.002

131 * When fitting all 8 test data samples to a single Hollomon equation. The corresponding n values are shown in Fig. 3.

132



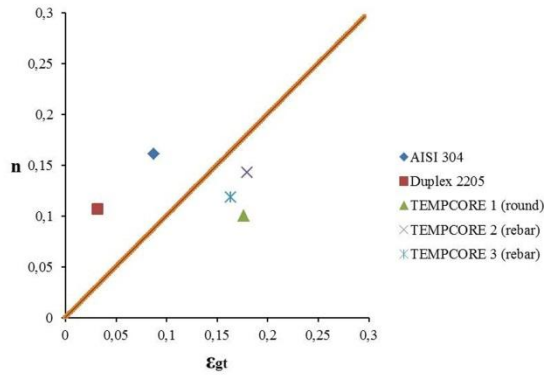
133

134 Figure 4. Log-Log graphs and best fit to Hollomon equation: (a) TEMPCORE[®] 1 (round); (b) TEMPCORE[®] 2 (rebar); (c)
 135 TEMPCORE[®] 3 (rebar); (d) AISI 304; and (e) Duplex 2205.

136

137 4. Discussion

138 According to Considère [29], ε_{gt} should equal n . By comparing the values of n and ε_{gt} in Table V or in Fig. 5, it becomes clear
 139 that these two values show no apparent connection.



140

141 Figure 5. Best fit n value vs. ε_{gt} for the materials tested

142 This apparently contravenes Considère [29] and Wiggly [41] criteria. Nevertheless, implicit to those criteria as stated in Eq. (3)
 143 and (4) is the assumption that the Hollomon function must include the maximum true stress point ($\varepsilon_{gt}, \sigma_m$). Given that the best
 144 fit has been computed by selecting the appropriate value of both K and n constants, that is, without such a boundary condition,
 145 there is no guarantee that this requirement will be fulfilled.

146 An additional issue arises from the fact that n values do change over the uniform plastic strain range. In fact, even though
 147 fitting quality is very good ($R^2 \approx 1$), it is convenient to notice that experimental data in Fig. 4 does not draw a constant slope
 148 shape. As pointed out previously, several authors have proposed that the hardening exponent value is sensitive to changing
 149 deformation mechanisms active at different strain levels. This is also valid for other metals, such as copper [42] and aluminium
 150 [43].

151 Local values of n can be computed after Rastegari [35] as follows:

$$152 \quad n_i = d(\ln \sigma_z) / d(\ln \varepsilon_z) = (d\sigma_z / \sigma_z) / (d\varepsilon_z / \varepsilon_z) = \left(\varepsilon_{zi} (\sigma_{z(i+1)} - \sigma_{z(i-1)}) \right) / \left(\sigma_{zi} (\varepsilon_{z(i+1)} - \varepsilon_{z(i-1)}) \right) \quad (6)$$

153 Fig. 6 displays the evolution of n as ε_z increases, for each of the eight samples of the five steel grades tested. A straight line
 154 representing the Considère equation (5) is also shown. Table VI lists maximum values of n , along with the n value on
 155 approaching ε_{gt} . Bearing in mind that experimental points were drawn up to σ_m , that is, ε_{gt} , it is clear that $n(\varepsilon_z \rightarrow \varepsilon_{gt}) \approx \varepsilon_{gt}$. Jacques
 156 [33] arrives at a similar conclusion for a 0.18% C plain carbon steel, slightly higher in Mn and Si compared to the
 157 TEMPCORE® steels tested in this paper.

158

Table VI. Characteristic values of the hardening exponent

	n_{max}	$n(\varepsilon_z \rightarrow \varepsilon_{gt})$	n_{mean}^*
TEMPCORE® 1	0.207±0.004	[0.996-1.043]	0.176±0.006
TEMPCORE® 2	0.191±0.003	[1.011-1.062]	0.180±0.004
TEMPCORE® 3	0.178±0.003	[1.013-1.070]	0.164±0.003
AISI 304	0.175±0.007	[1.004-1.028]	0.087±0.003
Duplex 2205	0.133±0.009	[1.005-1.373]	0.108±0.007

159 * From Table V

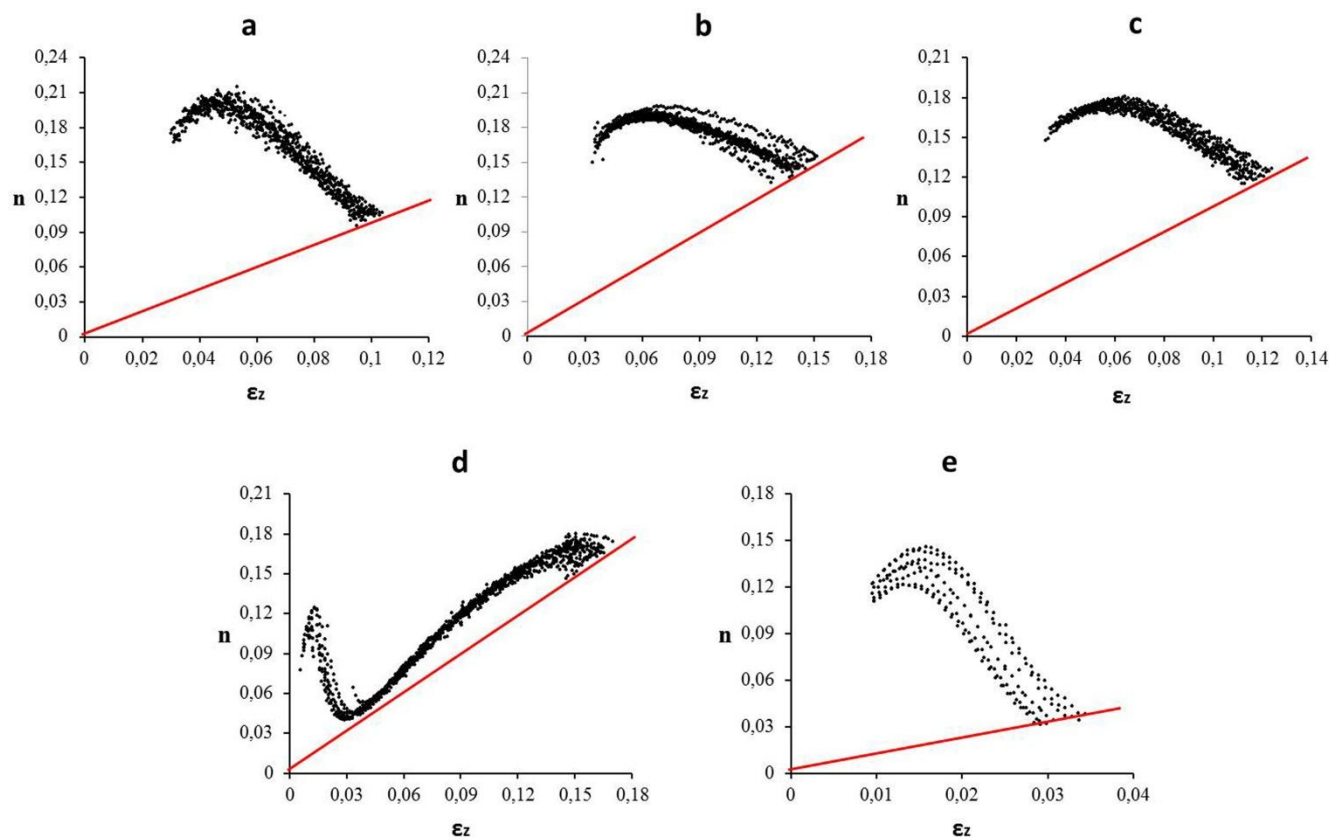
160 The evolution of the Hollomon hardening exponent as shown in Fig. 6 has major consequences. In the case where n is as low
 161 as $n(\varepsilon_z \rightarrow \varepsilon_{gt}) \approx \varepsilon_{gt}$ across the whole strain range, the probability of triggering an early necking would increase. On the other hand,
 162 the existence of an n value in the higher range would produce smaller differences between σ_m and σ_y . This is the case for
 163 carbon (ferritic-martensitic) TEMPCORE steels. Higher initial values of n allows a delayed beginning of necking by increasing
 164 the ductility of rebar. The values of ε_{gt} for these steels are between 0.1 and 0.15. Nevertheless, the final decreasing of n allows
 165 for a relatively standard-safe $R_m/R_{p,0.2}$ value, at higher than 1.2.

166 It is also interesting to note the behaviour of duplex (austeno-ferritic) stainless steel. In this particular case, n evolves in a
 167 similar way to that of carbon (ferritic-martensitic) steels. Nevertheless, maximum n values (around 0.14) are lower than those

168 found in ferritic-martensitic TEMPCORE[®] steels (over 0.18). Duplex steel presents ε_{gt} at around 0.03. Due to the appearance of
169 early necking along with the low Hollomon hardening exponent value, the $R_m/R_{p,0.2}$ value is therefore only approximately 1.1.

170 Finally, fully austenitic rebar behaves in a completely different pattern. At low strains, that is, below 0.03, the n vs. ε_z
171 relationship resembles that of duplex stainless steel. However, immediately before fulfilling the necking criteria by Considère
172 ($n=\varepsilon_z$), the n value increases and maintains just above the ε_z value. In this way, necking does not occur, thereby increasing the
173 value of ε_{gt} considerably by up to approximately 0.165. Since n values are relatively low across the uniform plastic strain
174 range, $R_m/R_{p,0.2}$, which lies in the range of 1.17, is not as high as with ferritic-martensitic materials.

175



176

177 Figure 6. Local hardening exponent at different plastic strain levels: (a) TEMPCORE[®] 1 (round); (b) TEMPCORE[®] 2 (rebar);
178 (c) TEMPCORE[®] 3 (rebar); (d) AISI 304; and (e) Duplex 2205. Experimental points of all the tested bars have been
179 represented.

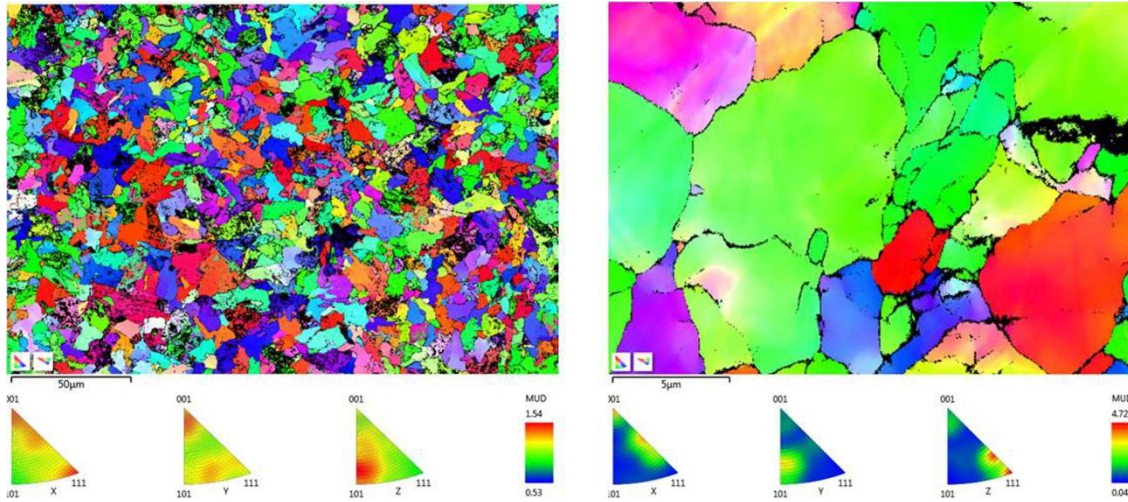
180 It is the aim of this paper to show that the Hollomon hardening exponent is not a constant and how this fact can affect the
181 ductility ($R_m/R_{p,0.2}$ and ε_{gt}) of various commercially available rebar materials. In this context, the authors consider that a basic
182 and preliminary look at the subjacent straining mechanism may give convenient insights for future research. Several authors
183 [30,31,44,45,46,47,48,49,50,51] have related hardening behavior to strain mechanisms and microstructures.

184 The definition of deformation mechanisms in carbon steel rebar is a difficult task. The core shows a low-carbon ferritic-
185 pearlitic structure. On the other hand, the outer coat of carbon steel rebar produced by TEMPCORE[®] process is composed of
186 tempered martensite. A transition zone, with bainite and other transformation structures, can also be found. Given that the
187 outer layer consists of a relatively small volume compared to the rebar volume ($\approx 16\%$), this paper will only focus on the
188 characterization of the core structure.

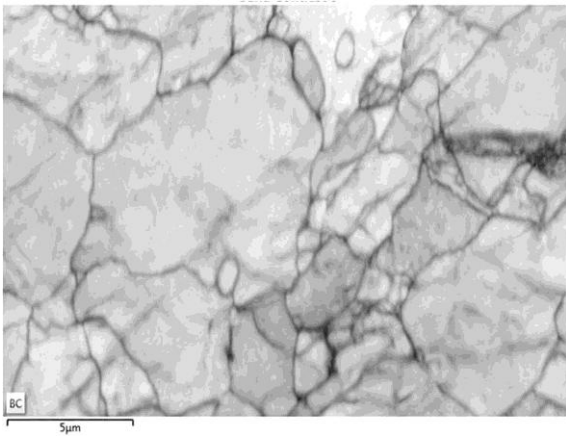
189 In order to characterize strain-related microstructural features, EBSD studies were carried out in ferritic (plain round
190 TEMPCORE[®] bar), austenitic, and austeno-ferritic steels. In order to find differences in steel structures at the beginning and

191 the end of the uniform straining period, two samples were prepared: before straining and at the onset of localized necking. The
192 EBSD Y axis corresponds to the direction of the tensile stress, while the X and Z axes are arbitrarily oriented Cartesian axes.

193 Fig. 7 shows IPF Y images and ferrite IPF projections for TEMPCORE[®] bar core before and after straining to ε_{gt} . The average
194 ferrite grain size is around 20 μm and diminishes to 8 μm after straining. Additionally, sub grain boundaries are evident after
195 straining (Fig. 8). Ferrite Y IPF projection shows no preferential orientation before straining, but for a slight (001) texture.
196 After straining to ε_{gt} , there is a notable increase of the number of grains that align their (101) direction to the Y tensile axis.



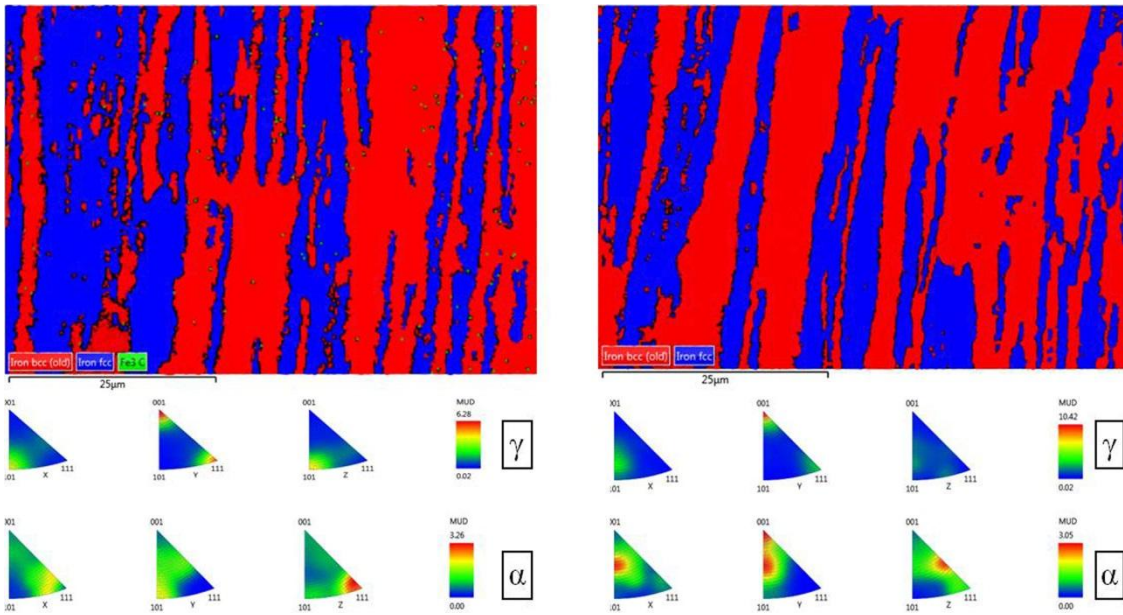
197
198 Figure 7. Ferrite EBSD data before (left-hand-side) and after (right-hand-side) straining to ε_{gt} .



199
200 Figure 8. Band Contrast image of TEMPCORE[®] rebar core after straining to ε_{gt} .

201 The hardening exponent value may be expected to decrease due to the grain refinement effect observed at $\varepsilon_z = \varepsilon_{gt}$ [30,47].
202 However, the probable increase in fresh-dislocation density and the sub grain formation will produce the opposite effect
203 [32,52]. Finally, the texture points towards the exhaustion of the partial deformation systems. According to said observations,
204 the decrease in the n value on increasing ε_z should be mainly attributed to grain refinement and the exhaustion of the
205 deformation systems. Promoting dynamic recrystallization may be a convenient approach to delay the decrease in the n value,
206 thereby increasing the value of ε_{gt} .

207 As can be deduced from Fig. 6 e), duplex steel presents a similar behaviour to that of TEMPCORE[®] rebar. Fig. 9 includes IPF
208 Y images and both ferrite and austenite IPF projections before and after straining to ε_{gt} .



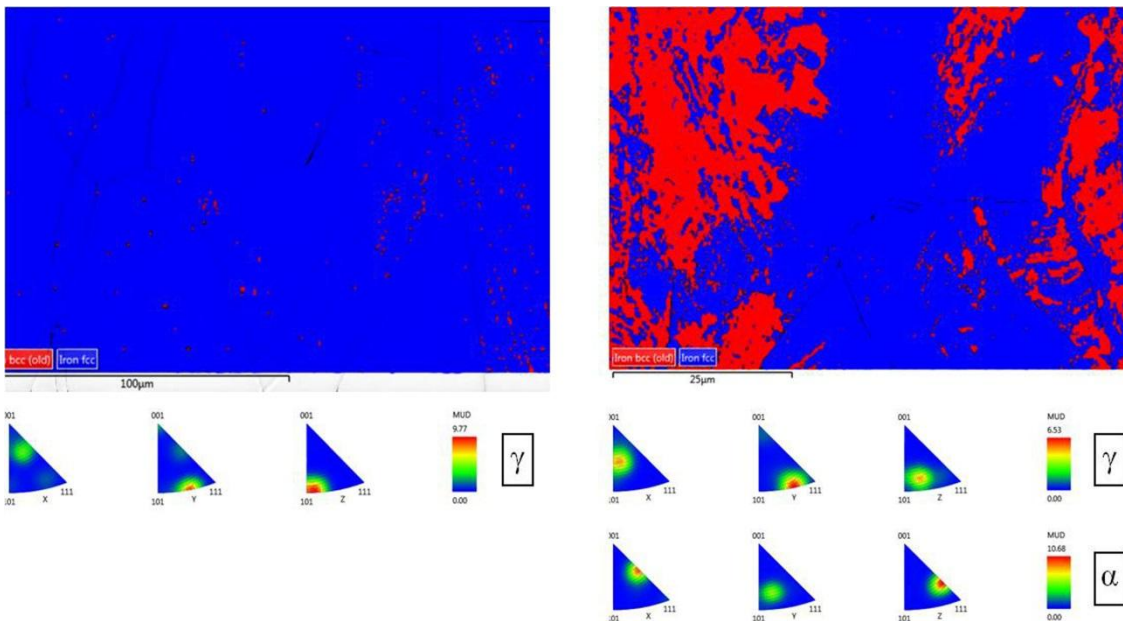
209

210

211 Figure 9. Ferrite and austenite EBSD data before (left-hand-side) and after (right-hand-side) straining to ϵ_{gr} .

212 The austeno-ferritic structure can be distinguished where austenite is shaped as stringers in a ferrite matrix. The relative
 213 amount of bcc structures increases slightly from 55.1 to 60.3% on straining to ϵ_{gr} . Before straining, the austenite appears
 214 slightly textured with a predominance of (001) and (111) directions parallel to the Y tensile axis. There is no clear evolution of
 215 austenite texture on straining to ϵ_{gr} . On the other hand, the ferrite phase experiences similar changes as with the TEMPCORE[®]
 216 steel. After straining, texturing in the (001) and (101) directions occurs. It can be said that the presence of austenite precludes
 217 an excessive ferrite crystal rotation, thereby preventing the activation of several (101)-(111) slipping systems. This gives lower
 218 n and ϵ_{gr} values for duplex steel. Fortunately, it is found that austenite deforms extensively after necking, and reaches rupture
 219 deformations in the same range as TEMPCORE[®]. Obviously this post-necking deformation is not desirable since concrete
 220 cannot accommodate these inhomogeneous strains without cracking.

221 Concerning austenitic steel rebar, the behaviour displayed in Fig. 6 clearly differs from the other materials. The austenite
 222 EBSD results are presented in Fig. 10. As can be seen, some austenite has transformed into martensite, which accounts for
 223 39.9% vol. on straining to ϵ_{gr} .



224

225 Figure 10. Austenite EBSD data before testing (left-hand-side). After straining to ε_{gt} , some austenite transforms into martensite
226 (right-hand-side).

227 Before testing, austenite grains are oriented from (101) to (111) crystal direction, aligning with the rolling direction. After
228 straining to ε_{gt} , it seems that such texture has not substantially changed. This behaviour conforms to that observed in the
229 austenitic phase of duplex rebar. In fact, n vs. ε_z evolution of both steels up to $\varepsilon_z \approx 0.03$ is very similar, as shown in Fig. 6.
230 However, from this strain value an increase in the n value begins, thereby preventing the condition $n = \varepsilon_z$, which would lead to
231 the appearance of localized necking. The mechanism proposed to explain such an increase in the n value is not exclusively a
232 plastic deformation mechanism. In fact, EBSD inverse pole figure projections show that no texture is apparent in the Y
233 direction due to straining for the γ , although the α phase does show a preferential orientation. In this context, strain-induced
234 martensitic structures show a higher specific volume than the parent austenitic phase. This increase is in the range of 10% and
235 it occurs mainly along the (101) martensite axis.

236 237 **5. Conclusions**

238 In this study, the work-hardening behaviour of rebar steel with different composition and microstructures is evaluated using
239 room-temperature tensile tests. The following conclusions can be drawn from this study:

240 (1) The value of the Hollomon hardening exponent, n , is dependent on the strain, probably as a result of varying deformation
241 mechanisms. The specific n - ε_z relationship is dependent on the specific rebar microstructure.

242 (2) The Considère criteria corollary, $n = \varepsilon_{gt}$, can be applied when $n(\varepsilon_z \rightarrow \varepsilon_{gt})$ value is considered, but it does not apply to the
243 mean n value.

244 (3) Carbon steel TEMPCORE[®] rebar shows a relatively high n value, which decreases on approaching the onset of necking.
245 This gives a convenient combination of high ε_{gt} and $R_m/R_{p,0.2}$ values.

246 (4) Duplex steel presents an n - ε_z relationship similar to that of carbon steel, but its n values are lower across the entire strain
247 range. Although deformation mechanisms may have certain similarities, both ε_{gt} and $R_m/R_{p,0.2}$ values are smaller than
248 TEMPCORE[®] rebar.

249 (5) Austenite rebar shows similar behaviour to that of duplex steel up to $\varepsilon_z \approx 0.03$. It has been shown that, by the onset of
250 necking, nearly 40% of the austenite has transformed into martensite. The additional volume increase may be responsible for
251 the observed additional increase of the hardening exponent. This enables even higher values of ε_{gt} than those of carbon steel
252 TEMPCORE[®] rebar to be attained.

253 **Acknowledgements**

254 The authors would like to acknowledge the contribution to the experimental work carried out by J. Pinto from the School of
255 Engineering, and R. Sánchez-Matos from the Polytechnic School, both of University of Seville.

256 **Bibliography**

- 257
- 258 [1] ISO 6892-1:2016, Metallic materials. Tensile testing. Part 1: Method of test at room temperature, International
259 Organization for Standardization (ISO/TC 164/SC 1), Ginebra, 2016.
 - 260 [2] ASTM E6-09, Standard Terminology Relating to Methods of Mechanical Testing, ASTM International, West
261 Conshohocken, PA, 2009.
 - 262 [3] P. Collins, Concrete: The Vision of a new Architecture, second ed., McGill-Queen's University Press, Québec, 2004.
 - 263 [4] E. L. Ransome, Patent Building Construction, United States, No. 305.226 A, 09/16/1884.
264 <http://www.google.com/patents/US305226> (accessed 12 August 2016).
 - 265 [5] F.J. San Emeterio, Armaduras pasivas en las estructuras de hormigón armado, Técnica Ind., 292 (2011).
 - 266 [6] G. Strohmeier, J. Bodem, Patent Rolls for rolling mills and method for making same, United States, No. 3974555 A,
267 08/17/1976, <http://www.google.com/patents/US3974555> (accessed 02 December 2016).

- 268 [7] Y. Zhao, R. Li, X. Wang, C. Han, Experimental research on seismic behaviors of precast concrete columns with large-
269 diameter and high-yield strength reinforcements splicing by grout-filled coupling sleeves, *China Civ. Eng. J.* 50 (2017)
270 27–35 and 71.
- 271 [8] J. Su, R. P. Dhakal, J. Wang, W. Wang, Seismic performance of RC bridge piers reinforced with varying yield strength
272 steel, *Earthq. Struct.* 12 (2017) 201–211.
- 273 [9] M. B. Sk, A. K. Khan, S. Lenka, B. Syed, J. Chakraborty, D. Chakrabarti, A. Deb, S. Chandra, S. Kundu, Effect of
274 microstructure and texture on the impact transition behaviour of thermo-mechanically treated reinforcement steel bars,
275 *Mater. Des.* 90 (2016) 1136–1150.
- 276 [10] J. Su, J. Wang, W. Wang, Z. Dong, B. Liu, Comparative experimental research on seismic performance of rectangular
277 concrete columns reinforced with high strength steel, *Journal Build. Struct.* 35 (2014) 20–27.
- 278 [11] X. Li, Z. Guo, Y. Rong, H. Wu, S. Yao, 600 MPa grade rebar with high ductility developed based on theory of yield
279 plateau, *Acta Metall. Sin.* 50 (2014) 439–446.
- 280 [12] D. M. Rice, J.R. Tracey, On the ductile enlargement of voids in triaxial stress fields, *J. Mech. Physic Solids* 17 (1969)
281 201–217.
- 282 [13] D.C. Rai, D.C., S.K. Jain, I. Chakrabarti, Evaluation of Properties of Steel Reinforcing Bars for Seismic Design, in
283 *Proceedings of the 15th World Conference on Earthquake Engineering* (2012), 21138–21147.
- 284 [14] H. Baji, H. R. Ronagh, A reliability-based investigation into ductility measures of RC beams designed according to fib
285 Model Code 2010, *Struct. Concr.* 16 (2015) 546–557.
- 286 [15] A. Charif, S. M. Mourad, M. I. Khan, Flexural behavior of beams reinforced with steel bars exceeding the nominal
287 yield strength, *Lat. Am. J. Solids Struct.* 13 (2016) 945–963.
- 288 [16] ISO 10606:1995, Steel for the reinforcement of concrete. Determination of percentage total elongation at maximum
289 force, International Organization for Standardization (ISO/TC 17/SC 16), Ginebra, 1995.
- 290 [17] ISO 6935-2:2015, Steel for the reinforcement of concrete. Part 2: Ribbed bars, International Organization for
291 Standardization (ISO/TC 17/SC 16), Ginebra, 2015.
- 292 [18] ASTM A615-16, Standard Specification for Deformed and Plain Carbon-Steel Bars for Concrete Reinforcement,
293 ASTM International, West Conshohocken, PA, 2016.
- 294 [19] BS 4449: 2005, Steel for the reinforcement of concrete weldable reinforcing steel, bar, coil and decoiled product,
295 British Standard Institute (ISE/104I), London, 2005.
- 296 [20] ISO 15630-1:2010, Steel for the reinforcement and prestressing of concrete. Test methods. Part 1: Reinforcing bars,
297 wire rod and wire, International Organization for Standardization (ISO/TC 17/SC 16), Ginebra, 2010.
- 298 [21] ASTM A370-17, Standard Test Methods and Definitions for Mechanical Testing of Steel Products, ASTM
299 International, West Conshohocken, PA, 2017.
- 300 [22] BS EN ISO 15630-1:2010, Steel for the reinforcement and prestressing of concrete. Test methods. Reinforcing bars,
301 wire rod and wire, British Standard Institute (ISE/104), London, 2010.
- 302 [23] ASTM E8-16, Standard Test Methods for Tension Testing of Metallic Materials, ASTM International, West
303 Conshohocken, PA, 2016.
- 304 [24] BS EN ISO 6892-1:2016, Metallic materials. Tensile testing. Method of test at room temperature, British Standard
305 Institute (ISE/101/1), London, 2016.
- 306 [25] Centre de Recherches Metallurgiques, Patent Tempcore, Norway, No. 520424, 07/20/1978.
307 <https://www.tmdn.org/tmview> (accessed 15 March 2016).
- 308 [26] B. Hortigón, J. M. Gallardo, E. J. Nieto-García, J. A. López, 2017. Elasto-plastic hardening models adjustment to
309 ferritic, austenitic and austenoferritic Rebar. *Rev. Metal.* 53, e094.
- 310 [27] X. Yun, L. Gadner, Stress-strain curves for hot-rolled steels, *J. Constr. Steel Res.* 133 (2017) 36–46.
- 311 [28] J. H. Hollomon, Tensile deformation, *Trans. Am. Inst. Min. Eng.* 162(1945) 268–290.
- 312 [29] M. Considère, L'emploi du fer et de l'acier dans les constructions, *Ann. des Ponts Chaussées* 9 (1885) 574.
- 313 [30] W.B. Morrison, The effect of grain size on the stress-strain relationship in low-carbon steel, *Trans. ASM.* 59 (1966)
314 824–846.
- 315 [31] A. Nouri, H. Saghafian, S. Kheirandish, Influence of volumen fraction of martensite on the work hardening behaviour
316 of two dual-phase steel with high and low silicon contents, *Int. J. Mater. Res* 101 (2010) 1286–1292.
- 317 [32] Y. Bergström, The Hollomon n-value, and the strain to necking in steel. (YBmat web, 2011), [http://www.plastic-](http://www.plastic-deformation.com/paper8.pdf)
318 [deformation.com/paper8.pdf](http://www.plastic-deformation.com/paper8.pdf). (accessed 18 May 2015)
- 319 [33] P. Jacques, X. Cornet, J. Ladrière, F. Delannay, Enhancement of the Mechanical Properties of a Low-Carbon, Low-
320 Silicon Steel by Formation of a Multiphased Microstructure Containing retained Austenite, *Metall. Mater. Trans. A* 29
321 (1998) 2383–2393.

- 322 [34] T. Xu, Y. Feng, Z. Jin, S. Song, Determination of the maximum strain hardening exponent, *Mater. Sci. Eng. A* 550
323 (2012) 80–86.
- 324 [35] H. Rastegari, A. Kermanpur, A. Najafizadeh, Effect of initial microstructure on the work hardening behavior of plain
325 eutectoid steel, *Mater. Sci. Eng. A* 632 (2015) 103–109.
- 326 [36] EN 1992-1-1 (2004): Design of concrete structures, European Committee for Standardization, Brussels, 1992.
- 327 [37] H. Castro, C. Rodríguez, F.J. Belzunce, Mechanical behaviour and corrosion resistance of stainless steel cold rolled
328 reinforcing bars, *Mater. Sci. Forum* 426-432 (2003) 1541-1546.
- 329 [38] E. Medina, J.M. Medina, A.Cobo, D.M. Bastidas, Evaluation of mechanical and structural behavior of austenitic and
330 duplex stainless steel reinforcements, *Constr. Build. Mater.* 78 (2015) 1-7.
- 331 [39] ASTM E112-13, Standard Test Methods for Determining Average Grain Size, ASTM International, West
332 Conshohocken, PA, 2013.
- 333 [40] A. Doñate, J. Calavera, J.M. Galligo, A.R. Marí, B. Perepérez, N. Gómez, N. Ruano: Diagramas característicos de
334 tracción de los aceros con características especiales de ductilidad, con marca ARCER, Monografías ARCER N° 4,
335 IPAC, Madrid, 2003.
- 336 [41] D. A. Wigley: Materials for low-temperature use, Oxford University Press for the Design Council, Oxford, 1978.
- 337 [42] A. Fattah-alhosseini, O. Imantalab, Y. Mazaheri, M.K. Keshavarz, Microstructural evolution, mechanical properties,
338 and strain hardening behavior of ultrafined grained commercial pure copper during the accumulative roll bonding
339 process, *Mater. Sci. Eng. A* 650 (2016) 8–14.
- 340 [43] S.O.Gashti, A. Fattah-alhosseini, Y. Mazaheri, M.K. Keshavarz, Effects of grain size and dislocation density on strain
341 hardening behavior of ultrafine grained AA1050 processed by accumulative roll bonding, *J. Alloys Compd.* 658 (2016)
342 854–861.
- 343 [44] F. Abbassi, S. Miston, A. Zghai, Failure analysis based on microvoid growth for sheet metal during uniaxial and biaxial
344 tensile test, *Mater. Des.* 49 (2013) 638–646.
- 345 [45] P. Antoine, S. Vandeputte, J.-B. Vogt, Empirical model predicting the value of the strain-hardening exponent of a Ti-IF
346 steel grade, *Mater. Sci. Eng. A* 433 (2006) 55–63.
- 347 [46] M. Homayonifar, M. Zebarjad, A. Sajjadi, A. Saatian, Investigation of the dependences of the mechanical
348 characteristics of an alloyed steel on both the strain rate and the microstructure, *J. Strain Anal. Eng. Des.* 42 (2007)
349 105–113.
- 350 [47] N. Bani, M. Ayaz, D. Mirahmadi, Statistical modeling of strain-hardening exponent and grain size of Nb-microalloyed
351 steels using a two-level factorial design of experiment, *J. Mater. Eng. Perform.* 22 (2013) 3337–3347.
- 352 [48] E. Candoni, M. Dotta, D. Forni, N. Tesio, C. Albertini, Mechanical behaviour of quenched and self-tempered
353 reinforcing steel in tension under high strain ratio, *Mater. Des.* 49 (2013) 657–666.
- 354 [49] P. Movahed, S. Kolahgar, S.P.H. Marashi, M. Pouranvari, N. Parvin The effect of intercritical heat treatment
355 temperature on the tensile properties and work hardening behavior of ferrite-martensite dual phase steels sheets, *Mater.*
356 *Sci. Eng. A* 518 (2009) 1–6.
- 357 [50] A. Ohmori, S. Torizuka and K. Nagai, Strain-hardening due to dispersed cementite for low carbon ultrafine-grained
358 steels, *ISIJ Int.* 44 (2004) 1063–1071.
- 359 [51] D. Tsuchida, N. Masudab, H. Harada, Y. Fukara, K. Tomota, Y. Nagai, Effect of ferrite grain size on tensile
360 deformation behaviour of a ferrite-cementite low carbon steel, *Mater. Sci. Eng. A* 448 (2008) 446–452.
- 361 [52] M. Kang, H. Kim, S. Lee, S.Y. Shin, Effects of dynamic strain hardening exponent on abnormal cleavage fracture
362 occurring during drop weight tear test of API X70 and X80 line pipe steels, *Metall. Mater. Trans. A* 45A (2014) 682–
363 697.
- 364

365

366